University of Glasgow

Higgins, R. J. , Zarev, A., Barakos, G. N. and Green, R. B. (2019) Numerical investigation of a two-bladed propeller inflow at yaw. *Journal of Aircraft*, 57(2), pp. 292-304. (doi:10.2514/1.C035647)

There may be differences between this version and the published version. You are advised to consult the publisher's version if you wish to cite from it.

http://eprints.gla.ac.uk/200795/

Deposited on 16 October 2019

Enlighten – Research publications by members of the University of Glasgow
http://eprints.gla.ac.uk

Numerical Investigation of a Two-Bladed Propeller Inflow at Yaw

Ross J. Higgins*, Angel Zarev†, George N. Barakos‡, Richard B. Green§
University of Glasgow, James Watt South Building, Glasgow, G12 8QQ, U.K.

The development of faster computing power and non-intrusive experimental techniques, have allowed for the advancement in Compuational Fluid Dynamic (CFD) validation and the greater understanding of aerodynamic conditions previously deemed too extreme to accurately measure. To this end, a numerical study is conducted which focuses on a propeller at yaw. Current low order methods are reliant upon an accurate inflow profile to determine overall blade loading patterns. In order to improve such methods, CFD can be used to determine an initial inflow profile from which to conduct additional lower-order calculations. Therefore, to ensure CFD is able to accurately capture yawed inflow profiles, a validation study is conducted which compares numerical simulations against experiments. Good agreement is found between the two methods and subsequently, the azimuthal variation in skin friction and induced angle of attack, as a result of the yawed conditions, is analysed.

Nomenclature

Latin

A	=	Propeller Disc Area (m^2)
c_{ref}	=	Blade Chord (m)
IF	=	Induction Factor Coefficient (-)
k	=	Turbulence Kinetic Energy (m^2/s^2)
T	=	Thrust (N)
R/c	=	Blade Aspect Ratio (-)
V_∞	=	Freestream Velocity (m/s)
V_i	=	Induced Velocity (m/s)
$\bar{V_i}$	=	Averaged Induced Velocity (m/s)

Greek

*PhD Student, r.higgins.1@research.gla.ac.uk
†PhD Student, a.zarev.1@research.gla.ac.uk
‡Professor, george.barakos@glasgow.ac.uk ,corresponding author.
§Senior Lecturer, richard.green@glasgow.ac.uk

ρ = Density (kg/m^3)

ω = Specific Rate of Dissipation (1/s)

$\vec{\omega}$ = Vorticity (1/s)

Introduction

Computational Fluid Dynamics (CFD) is nowadays used for the analysis and design of all rotary wings. Application examples can be found for propellers [1], helicopter rotors [2], wind turbines [3] and aero-engines [4] covering a range of operating conditions. Such investigations provide insights into complex aerodynamics and how rotating blades can be manipulated to deliver efficient operations. The validation of the CFD predictions against wind tunnel data is also progressing with new experimental methods providing detailed measurements on and off the lifting surfaces. This article presents such an example where measurements for the inflow of a propeller are used for CFD validation. This is in contrast to other validation studies for propellers [1] where acoustics, wakes or surface loads are of interest. This article is using recent Laser Doppler Anemometry (LDA) data obtained at the University of Glasgow wind tunnel facilities which focused on the measurement of propeller inflow profiles at yaw [5].

One of the reasons behind the experimental investigation was to provide a modern set of test data available for propellers at yaw, as very few experimental data sets existed in the public domain. Several of these works were conducted pre-World War 2 [6–11] and focused on the measurement of averaged forces and moments in order to determine aircraft stability and performance. Durand [7] found that at large yaw angles, the thrust coefficient was seen to increase significantly with advance ratio and blade pitch. This conclusion was verified by Flachsbart [8] whom expanded on the work of Durand by obtaining results for the lateral force and yaw moment. It was also found by Freeman [9] that no major efficiency reduction was seen when a propeller is at yaw.

A greater amount of work was conducted post-World War 2 [12–17] which focused on a larger variety of factors, including structural effects and wake aerodynamic composition. The initial works of Pendley [13] and Russell [15, 16] found there to be discrepancies between the analytical and experimental loads. Conclusions drawn from these studies found there to be an azimuthal shift in the propeller wake potentially impacting the derived loads. The later studies by Gray [12], McLemore [14] and Yaggy [17] found oscillating airloads to have a significant impact when the propeller is at yaw.

While being informative of some basic trends, the information in those studies is constrained by a number of factors. These include, but are not limited to, restricted temporal and geometric data resolution, lack of a well populated experimental envelopes in some cases, and limited data accuracy. With the development of non-interfering techniques, such as LDA, an opportunity for a better understanding of propellers at yaw is available.

In terms of numerical models, it is found that many of the widely available low order solvers still work under the assumption of uniform induced flow across the propeller disc, set out by de Young in 1965 [18], or the steady-state assumption defined by Crigler in 1952 [19]. An improvement on these models was derived in 1980 by Pitts and Peters [20, 21], where the induced velocity at the propeller plane is calculated based upon a truncated Fourier series and works under the assumption of the superposition of pressure. Studies have been conducted in recent times [22] with consistent results of forces and moments found in axial and yawed test conditions whilst using the Pitts and Peters model. The Pitts and Peters is a dynamic inflow model and it requires additional coupling to a blade element like model in order to obtain propeller blade loads. Such a model can provide an accurate solution at a low-order cost, however, it is reliant upon an accurate initial solution. With the development of faster computing power, full three-dimensional (3D) CFD can be utilised for the study of propeller inflow profiles.

Due to the development of CFD in recent times, trust has been gained in such tools. As a result, CFD can be used to obtain propeller inflow profiles for subsequent use in lower order methods. The inflow profile can often be critical in the overall accuracy of such methods. An instant where the standard assumptions fail is for a propeller at yaw. Therefore, in order to ensure CFD is able to accurately capture the inflow profiles, a validation study is conducted against experiments. The study validates against axial and yawed conditions, with a grid and turbulence model convergence procedure conducted. One of the benefits of modern CFD is the ability to gain greater insight into the physics behind different aerodynamic conditions. To this end, the effect of yaw on the blade induced angle of attack and skin friction is analysed.

Computational Methodology

For the numerical investigation into propeller flows at yaw, the in-house CFD solver Helicopter-Multi-Block-3 (HMB3) is used. The core functionality of HMB3 is CFD, however its use has been extended in recent years to include whole engineering applications, including helicopter rotor aeroelasticity[23], propeller aeroacoustics[1], flight mechanics[24] and missile trajectory prediction[25]. Previous investigations using HMB3 have provided propeller flow validation in both installed and isolated conditions, by comparison with the experimental results of the Joint Open Rotor Propeller (JORP) blade [26] and the Improving the Propulsion Aerodynamic and aCoustics of Turboprop Aircraft (IMPACTA) wind tunnel tests [27, 28]. These results were compared in 2016 [29] and 2018 [1], respectively, with good agreement found in terms of aerodynamics and acoustics.

Numerical Setup

This investigation uses a laser scan of the experimental two-bladed propeller. The blade is of a generic design, with the main usage being for model aircraft from weight class $8kg$ to $25kg$. It is a $49.9cm$ diameter blade of weight $54g$ with the blade specification presented in Figure 1.

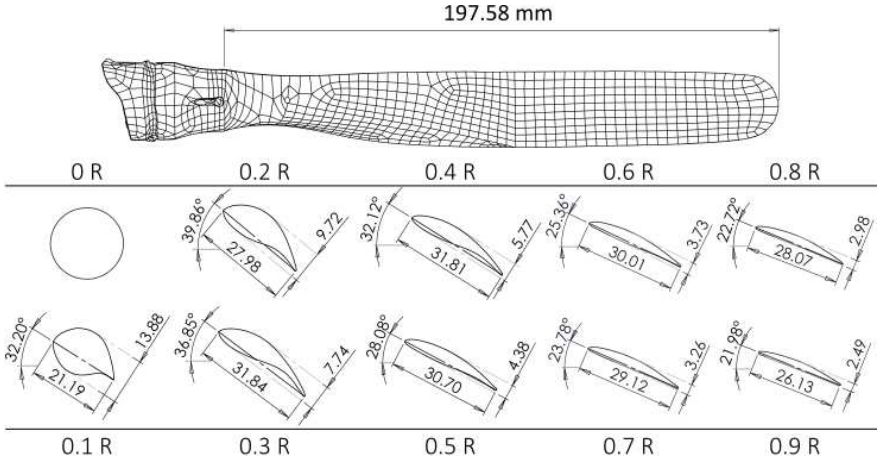

Fig. 1 Blade Specification

The numerical study focused on the mid-range propeller conditions presented in the experimental investigation, with the freestream velocity of 20 m/s, rotational velocity of 2756 ($r\ pm$), and blade pitch angle of 28° selected. The blade pitch was measured using an inclinometer during the experiment with a tolerance of ±0.1°. The freestream velocity, rotational velocity and blade pitch were adjusted in tandem during each sweep of yaw angles. To highlight the differences found in inflow conditions, the axial flow and 20° yaw conditions were investigated. The 20° yaw condition is selected for computational analysis due to it being the most extreme of yawed cases from the experimental study. The yaw angle range from 0° to 20° was selected during the experiment as these angles were seen to be relevant for all propeller based applications with higher angles only observed for tiltrotor aircraft.

For axial flow conditions, periodicity in space and time is assumed. This allows for a reduction in computational cost due to the inclusion of the rotational source term in the Reynolds-Averaged Navier-Stokes (*RANS*) equations. From this, an unsteady solution is derived from a steady computation. In yawed flow conditions, periodicity in space and time can no longer be assumed due to the non-uniformity of the freestream conditions. As a result, Unsteady Reynolds-Averaged Navier-Stokes (*URANS*) simulations using the entire propeller is required. For this simulation the source term is set to zero.

Mesh Generation Techniques

This investigation requires the relative motion of the propeller blade. To achieve this, the chimera method is used[30]. The chimera method is based on composite grids, consisting of independently generated, overlapping non-

matching sub-domains. Each of these sub-domains are referred to as a Levels and are sorted hierarchically, with higher levels having priority. The exchange of information between sub-domains is achieved through interpolation and by following a hierarchy of mesh levels [30]. This allows for a mesh level to be defined around the propeller blade, thus applying the relative motion to the propeller. ICEM-Hexa™ of ANSYS is used to generate all grids.

For the axial flow case, a single blade, 180°, domain is created with a radial distance from the origin set as 7 R/c. The domain inflow and outflow were set as 5 R/c and 11 R/c from the origin, respectively, shown in Figure 2(a). Periodic boundary conditions are applied to the highlighted block faces with far-field boundary conditions applied to the remaining extreme faces.

No relative motion is required for the axial flow case, however, the chimera method is still used as this allows for the same blade foreground grid to be used on both simulations. The blade foreground grid is presented in Figure 2(b). In order to reduce blocking complexity, the blade was cut at the 20% radial station. This removes the need for a detailed grid around the blade cylindrical section where hub mounting structures are located. In addition to this, the inflow measurements during the experiment started from the 20% radial station, therefore no data is available for comparison below 20% radius. A radial slice of the foreground mesh can be seen in Figure 2(b), where the number of grid points around the 60%R aerofoil section is detailed. The normal edges to the aerofoil section are clustered towards the blade, using a hyperbolic law, to a spacing of $1 \times 10^{-5}\, c_{ref}$. A total of 29 nodes are used to distribute the cells normal to the aerofoil towards the chimera boundary, with a total of 110 cells distributed around the blade section. An O-grid topology was used for the blade foreground as this allowed for the even distribution of blocks around the blade tip and blunt trailing edge. A total of 184 nodes are distributed along the blade radius, clustering towards the tip and root. Overall, the total baseline grid size of the blade foreground is 606, 400 cells.

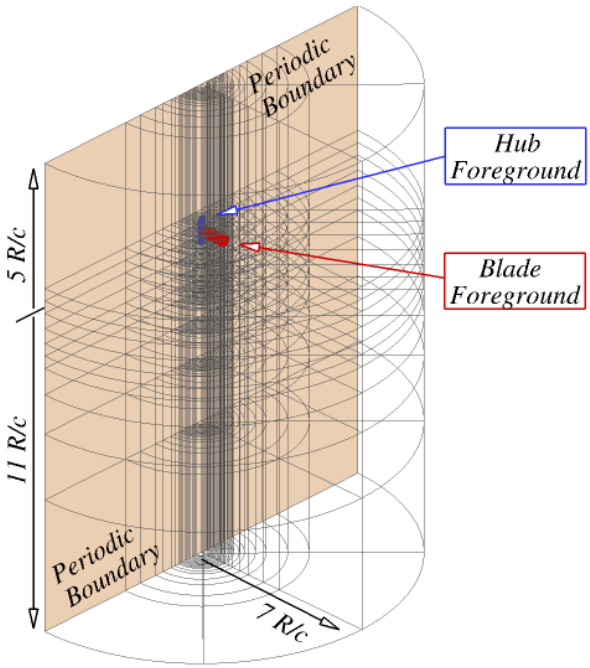

(a) Axial Computational Domain

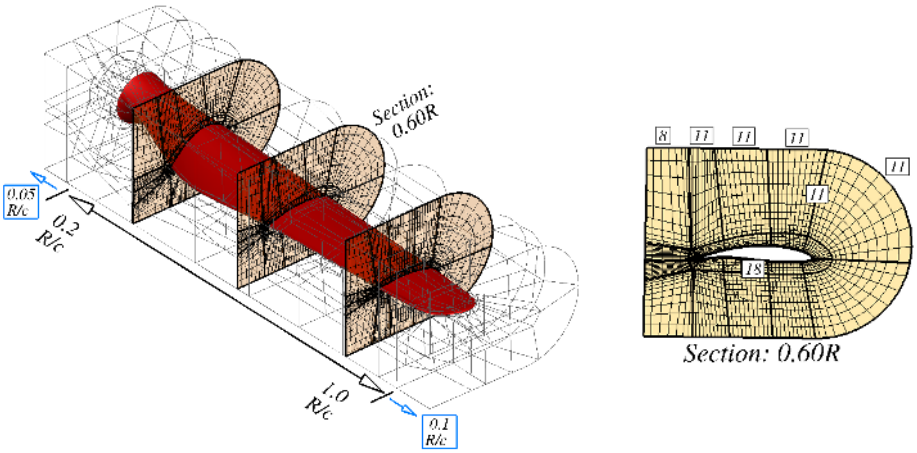

(b) Blade foreground grid for both axial and yawed computations

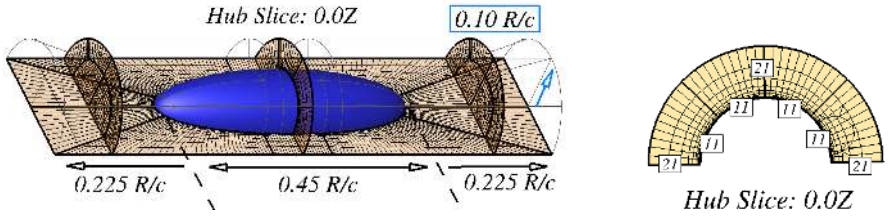

(c) Hub foreground grid for both axial and yawed computations

Fig. 2 Axial flow computational domain and foreground grid detail.

In addition to the propeller blade, the computational hub was included as a foreground level. This was done in order to reduce the computational complexity of the background grid. The computational hub geometry is derived using the leading edge curvature of the NACA 0016 for the fore and aft components, combined with a cylindrical centre station to provide a total axial length of 0.45 R/c. The inflow and outflow chimera boundaries were selected to be half the hub axial length away from the hub, with a radial distance of 0.1 R/c selected. An O-grid blocking topology is used, with all normal edges clustering to $1 \times 10^{-5}\, c_{ref}$, as per the blade foreground. The total baseline grid size for the computational hub is 83, 200 cells.

For the background grid, a standard cylindrical blocking structure is used. The background cells are clustered towards the propeller blade in all directions in order to ensure efficient interpolation between foreground and background grids. Overall, the baseline background grid has 12, 053, 856 cells. This results in an overall grid size of 12, 743, 456 cells for the axial computations.

Due to the efficiency of the axial flow setup, the yawed computation simply requires the transformation of the axial grid into the full 360° domain. A tolerance of 0.001 c_{ref} is selected for the matching of the periodic boundaries. The only change to the grid levels comes from the background. The foreground levels, the hub and blade, remain the same. In order to ensure the same level of interpolation between the blade foreground and background, the background cells no longer cluster tangentially towards the blade in the 0° azimuth position. The number of tangential cells within the

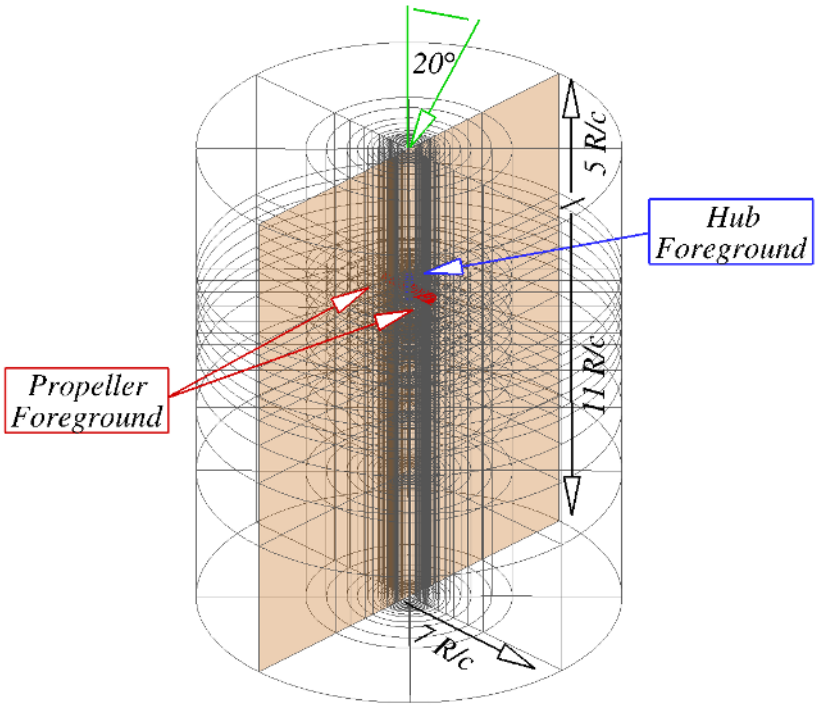

Fig. 3 Yawed flow computational domain.

block adjacent to the periodic boundaries was increased to ensure a uniform distribution of cells around the azimuth. This results in a baseline background grid of $19,964,000$ cells, for the entire domain. In total, the baseline yawed computational grid has $21,343,200$ cells.

Test conditions

As previously stated, the test conditions for the axial flow case were selected to be the mid-range parameters from the experimental study. Table 1 details the axial flow test conditions. For the axial flow computation the blade tip Mach number is required with the Reynolds number also referencing the tip conditions.

Tip Reynolds Number (-)	0.142×10^6
Tip Velocity *(m/s)*	70.71
Propeller Rotational Velocity *(rpm)*	2756
Inflow Velocity *(m/s)*	20.0
Ambient Temperature ($^\circ C$)	7.5
Speed of Sound *(m/s)*	335.8
Blade Pitch Angle $(^\circ)_{0.70R}$	28
Reference Chord Length *(mm)*	21.19
Blade Radius *(m)*	0.245

Table 1 Summary of the axial flow test conditions.

During the experiments, the propeller blade yaw angle was adjusted with respect to the freestream for the ease of the experimental setup. The opposite is found in the computation where, for the ease of computational setup, the freestream yaw angle is adjusted. This is highlighted in Figure 3. The test conditions for the yawed case are presented in Table 2. The azimuthal time-step for the yawed simulation was selected as 1.0°, with a reduced frequency of 0.1529. The reference Mach number and Reynolds number for the unsteady simulation are taken from the freestream inflow velocity.

Freestream Reynolds Number (-)	0.025×10^6
Tip Velocity *(m/s)*	70.71
Propeller Rotational Velocity *(rpm)*	2756
Inflow Velocity *(m/s)*	20.0
Inflow Yaw Angle (°)	20.0
Ambient Temperature ($^\circ C$)	10.05
Speed of Sound *(m/s)*	337.32
Reduced Frequency (-)	0.1529
Time-step ($^\circ/step$)	1.0
Blade Pitch Angle $(^\circ)_{0.70R}$	28
Reference Chord Length *(mm)*	21.19
Blade Radius *(m)*	0.245

Table 2 Summary of the 20° **yaw test conditions.**

Inflow Grid Location

The examined inflow resolution is as per the experimental study: 10 radial stations; 10° azimuth resolution; 3*cm* upstream of propeller. This is highlighted in Figure 4(a). The upstream location of 3*cm* was selected in order to avoid reflections of the LDA lasers and the experimental assembly (the hub geometry extruded upstream of the propeller mounting location). In line with the experimental study, the examined inflow grid centre is adjusted with respect to the yaw angle for the yawed flow case. The radial and azimuth resolution is kept constant, along with the normal distance to the grid. This is seen in Figure 4(b).

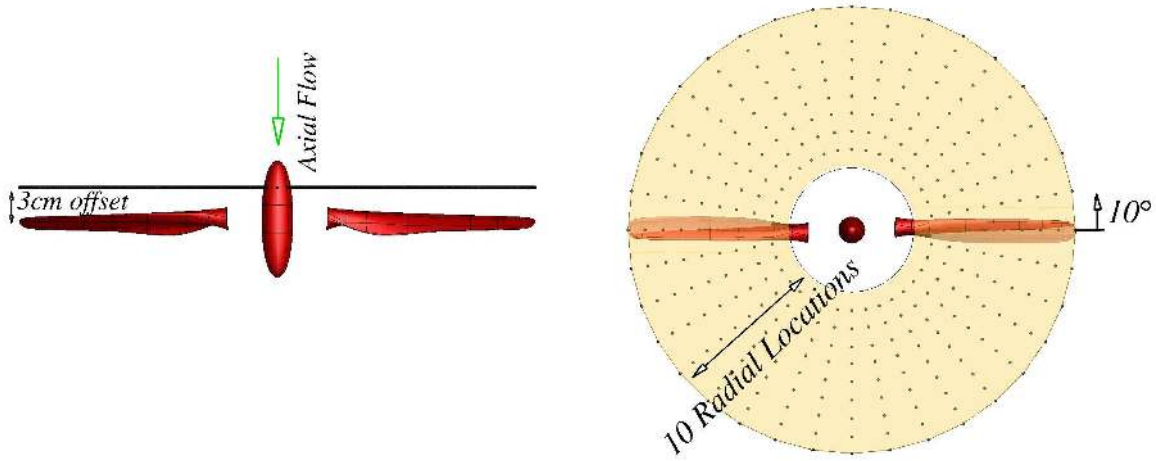

(a) Axial flow grid

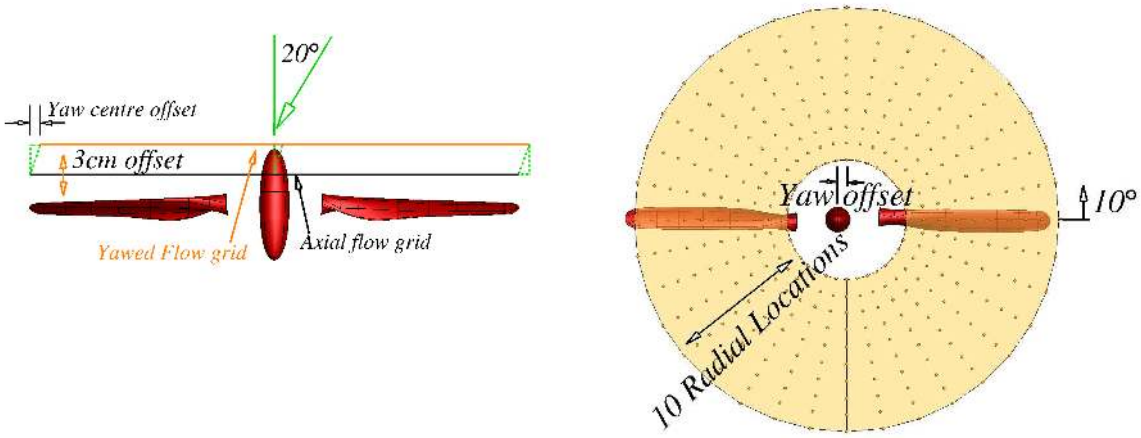

(b) Yawed flow grid

Fig. 4 Inflow grid location and resolution for the axial and yawed flow test cases.

Numerical Results

Presented below are the numerical results obtained using HMB3. A comparison is performed in terms of the inflow conditions, with additional flow-features highlighted.

As per the experimental study, the effect of propeller inflow is examined via Induction Factor (IF) coefficients. This is simply the ratio of the induced velocity profile to the freestream inflow velocity (Equation 1).

$$IF = \frac{V_i}{V_\infty}, \tag{1}$$

where V_i is the induced velocity calculated from the subtraction of the install velocity (propeller-off) from the propeller-on value. For the numerical study, the install profile is simply the freestream conditions.

Grid Convergence

To ensure confidence in the numerical solution, a grid convergence study was conducted using the yawed test conditions shown in Table 2. For this study, a coarser grid of $3,832,000$ cells was derived for the yawed flow computation. This is a 82% reduction in cell count when compared to the baseline grid of $21,343,200$ cells.

Presented in Figure 5 is the difference in induction factor coefficients between the coarse and baseline grids. The same trends in induction factors are observed for both grids, therefore the differences between the results are examined. The values in Figure 5 are weighted with respect to the average axial induction factor.

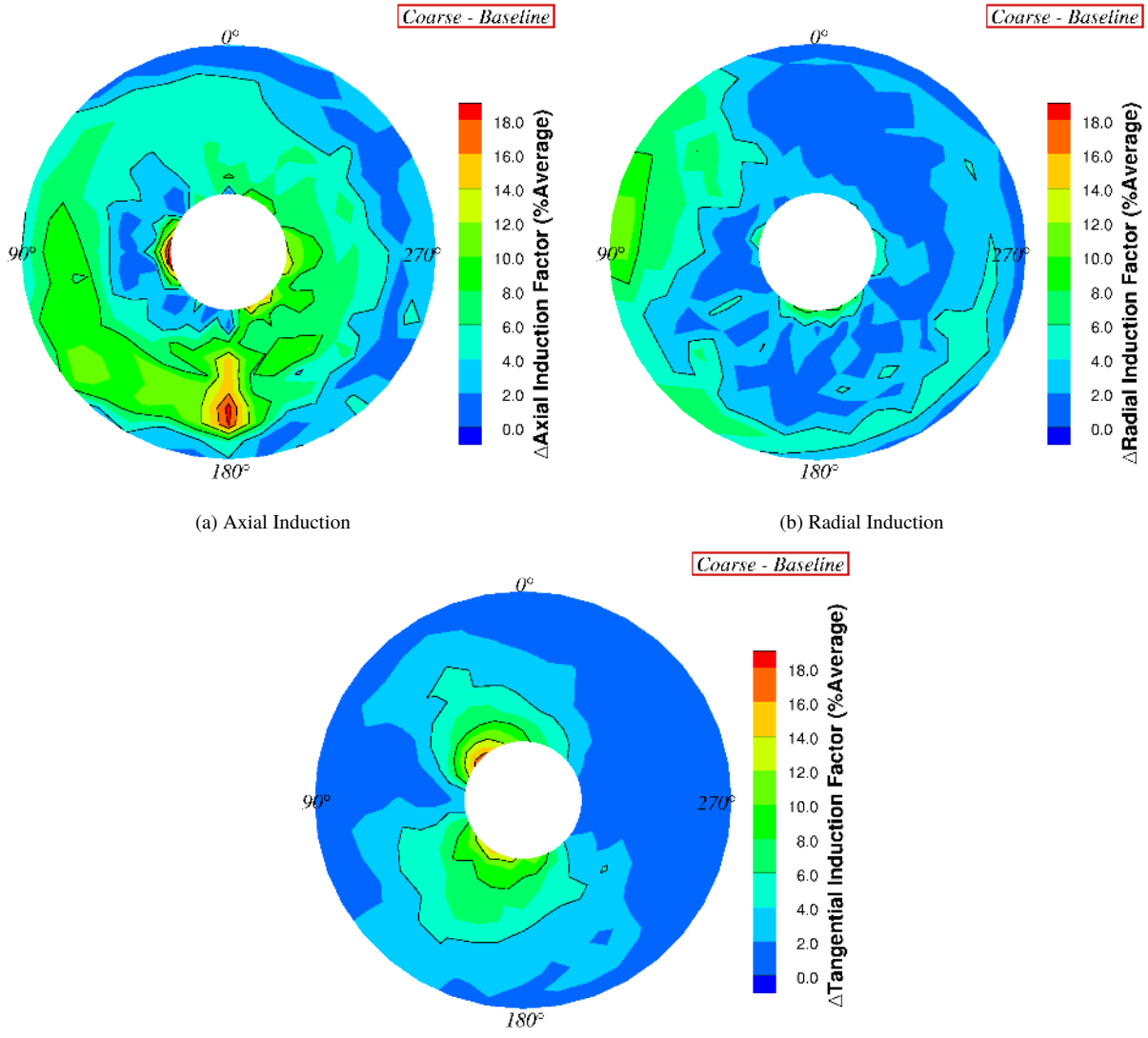

(a) Axial Induction

(b) Radial Induction

(c) Tangential Induction

Fig. 5 Change in the induction factor coefficients between the coarse and baseline grid. All values are weighted with respect to the average axial induction.

Local changes between the baseline and coarse grids are observed. An 18% change in axial induction is observed at 180° and 90°, with an overall increase seen between these azimuthal stations. At the 90° azimuthal station, the radial induction for the coarse grid increases by 8%. For the tangential induction, differences of more than 8% are observed around 50° and 150°, with the maximum change seen around 50°.

Table 3 presents a summary of the average induction factor components for the coarse and baseline grids, along with the percentage differences. As observed, all components decrease in magnitude from coarse to baseline grid. Larger percentage differences are found for the radial and tangential components, however, if these values are scaled by the baseline axial value due to the axial component being the most dominant, all percentages are seen to change by less than 5%.

Component	*Coarse*	*Baseline*	*% Difference*	*Axial Weighted % Difference*
Axial	0.04433	0.04267	3.8	3.8
Radial	-0.01828	-0.01638	11.6	4.45
Tangential	0.00058	0.00036	61.2	0.5

Table 3 Average induction factor values for the coarse and baseline grid.

Coupled with the levels of induced velocity is the generated loads. A comparison of the change in vertical load and pitching moment is presented in Figure 6. These load results are calculated based upon the computational surface pressure. As can be seen, very little change is observed between the two grids. On average, there is a 0.034% change in vertical load and a 0.016% change in pitching moment across the disk. These results, along with the weighted induction factor values, gives confidence that a converged solution is achieved with the baseline grid and, hence, will be used for the remaining computations.

Comparison of Standard *URANS* and Scale-Resolving Methods

Following the agreement in results from the grid convergence study, a comparison is made between the standard *URANS* formulation and the scale-resolving, hybrid *URANS-Large Eddy Simulation* method, Scale-Adaptive Simulation (*SAS*). For the *SAS* formulation, an additional source term is added to the $k-\omega$ Shear Stress Transport (SST) equations which allows for the local adjustment of the von-Karman length scale and balances the contributions from resolved and statistical components. The *SAS* formulation in HMB3 has been used in the past for transonic cavity flows [31], missile projection [32] and stall flutter predictions [33]. This investigation was conducted to ensure that the standard *URANS* formulation closed with the $k-\omega$ turbulence model is accurate enough to capture the correct physics.

As per the grid convergence study, the same trends between the *URANS* and *SAS* formulations are observed, therefore, the difference in inflow values are presented in Figure 7. A reduction of around 8% is observed around the 180° azimuthal station for the axial induction component. This reduction brings the simulation value closer to

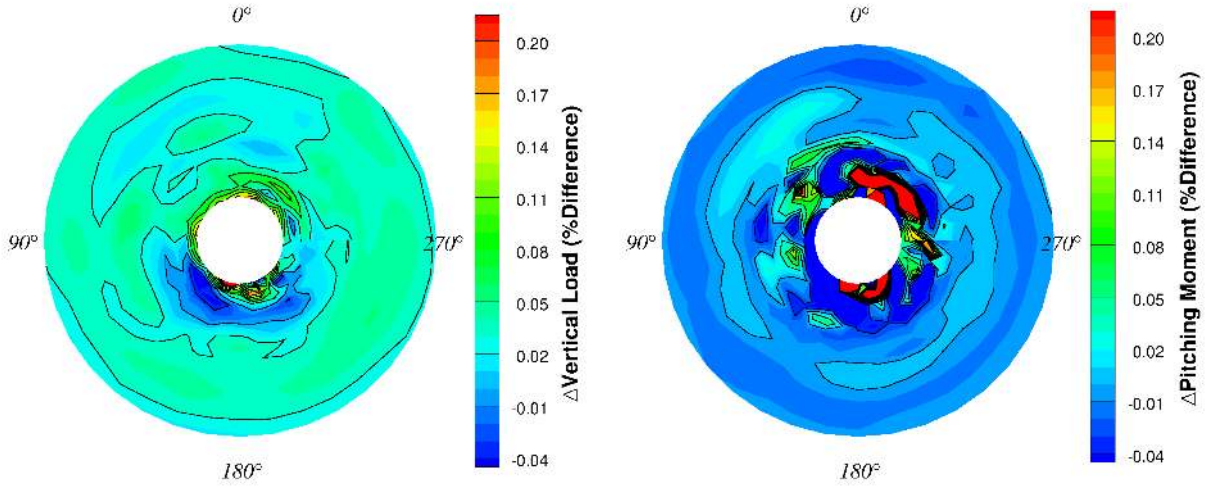

(a) Vertical Load

(b) Pitching Moment

Fig. 6 Change in vertical load and pitching moment coefficients between the coarse and baseline grids.

the experiment. For the radial induction factor, an increase of around 7% is observed between 180° and 360° (0°). Virtually no change is observed in the tangential induced velocities.

The average induction factor values, and the percentage differences, are presented in Table 4. As observed, the individual component percentages have reduced when compared to the grid convergence study, with all percentages halved in value.

Component	*SAS*	*URANS*	*% Difference*	*Axial Weighted % Difference*
Axial	0.04222	0.04267	1.07	1.07
Radial	-0.01529	-0.01638	6.65	2.55
Tangential	0.00024	0.00036	32.38	0.27

Table 4 Average induction factor values for the *URANS* and *SAS* simulations.

In addition to the induction factors, a comparison of the spanwise loads was conducted. For the vertical load, an average percentage change of 0.012% was seen, with a 0.066% change in the pitching moment coefficient. Based upon these results, it is clear that the standard *URANS* formulation with the $k-\omega$ turbulence model is sufficient to capture the yawed flow test case.

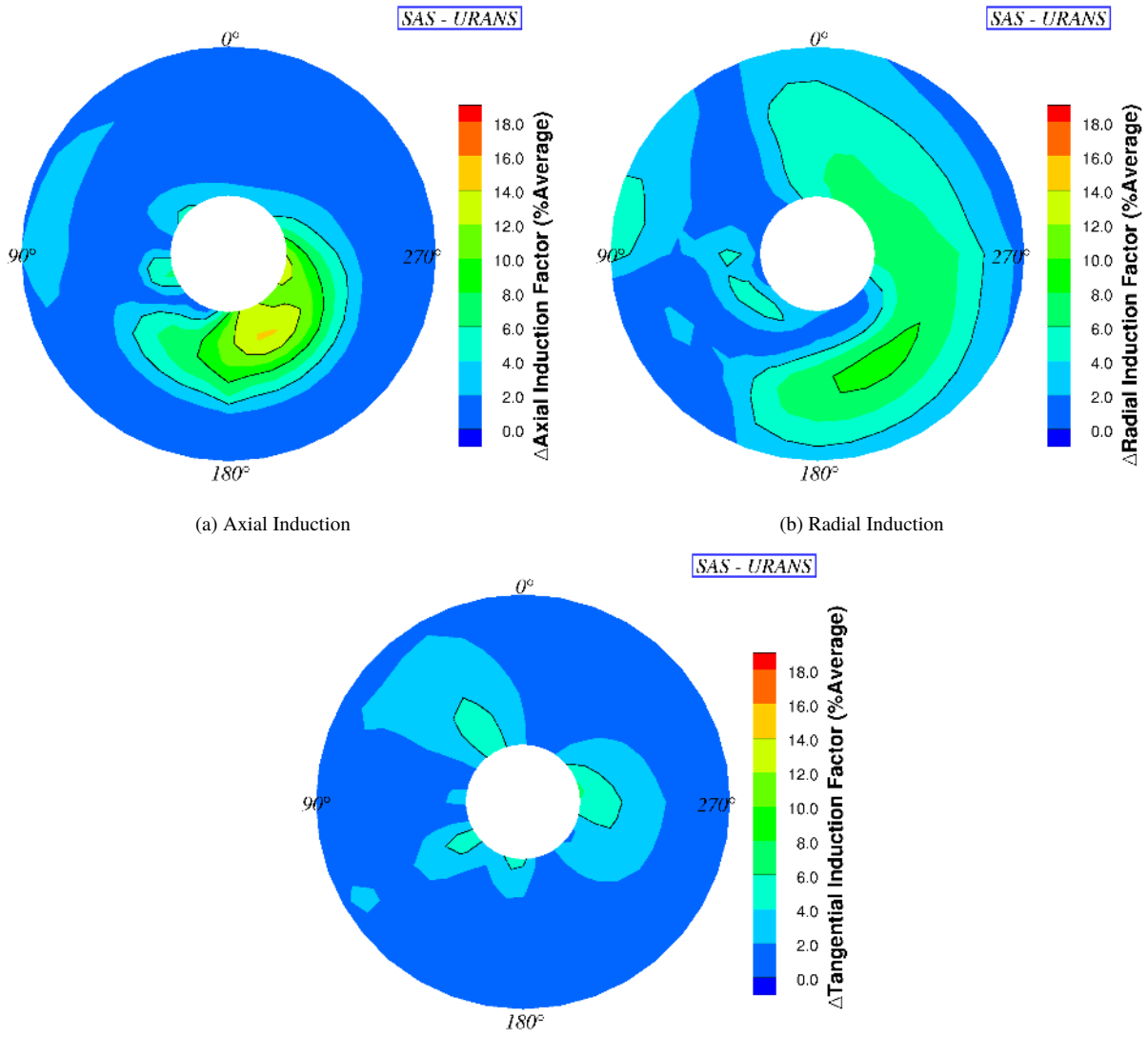

(a) Axial Induction

(b) Radial Induction

(c) Tangential Induction

Fig. 7 Change in the induction factor coefficients between the *URANS* and *SAS* methods. All values are weighted with respect to the average axial induction.

Axial Flow Conditions

Following the grid convergence and turbulence modelling study, a comparison is made to experimental data. Presented in Figure 8 is the comparison of the axial induction factor for the axial flow test case. Good agreement is found between the experiment and computational data. As expected, a uniform velocity profile is observed in both experiments and simulations. A 20% increase in the maximum axial induction is found for the simulation. The average induction factor found from the experiment is found to be 0.0349. This increases for the simulation to 0.0440, an increase of 26%. From the experiment, a small amount of negative induction is present towards the blade root which is

not observed within the CFD. This negative induction is a result of the experimental hub structure having a significant influence on the flow features within this region. This results in a higher change in induction of 0.0603, as compared to 0.0377 from the CFD.

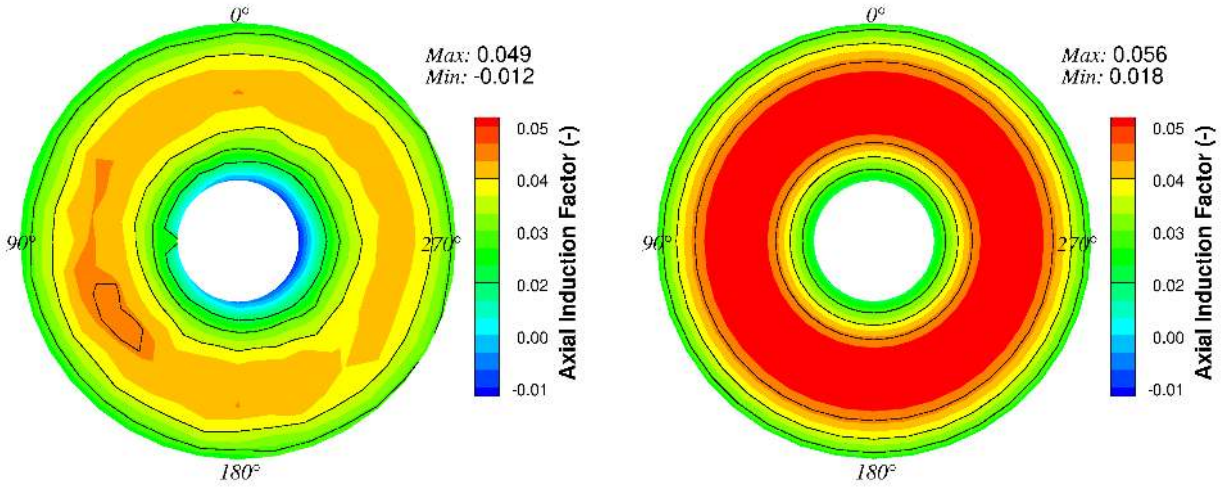

(a) Experiment (b) CFD

Fig. 8 Comparison between the experimental and numerical study of the axial induction factor for the axial flow test case.

The following set of experimental data did not contain any indication of the thrust produced from the propeller blade. In order to fully compare the inflow profiles, the same level of thrust must be observed between the experiment and CFD. To this end, the amount of thrust is estimated based upon momentum theory for a rotor in axial flight:

$$T = 2\rho A \left(V_\infty + \bar{V}_i\right) \bar{V}_i, \tag{2}$$

where $\bar{V}_i$ is the average induced velocity across the propeller disk and V_∞ is the freestream velocity. The averaged induced velocity is calculated based upon the average induction factor, thus resulting in a phase-averaged solution. The experimental thrust is estimated to a value of 6.68 N, with the CFD found to be 27% higher at 8.49 N. No thrust variations are observed with the propeller in axial flow.

Following this, iterative simulations were conducted with a reduced pitch angle in order to match the level of thrust and to improve the correlation between experimental and computational inflow profiles. Presented in Figure 9 is the comparison between the experimental data and the axial flight simulation for a reduction in pitch of 2.5°. As can be seen, an improved correlation is found between the CFD and experimental data. The average induction factor for the CFD is reduced by 25% to 0.0354, 1% higher than the experimental data value of 0.0349. In terms of thrust, this relates to a 25% reduction in thrust to 6.79 N, 1% off the estimated experimental thrust coefficient value of 6.68 N. Due to the adjustment of the freestream velocity, rotational velocity and pitch angle in tandem for the experiment, no specific

trend between the reference pitch angle and CFD adjustment can be made. The reason behind the higher values of induced velocity for the CFD are down to experimental installation and the laser scanning effects of the geometry.

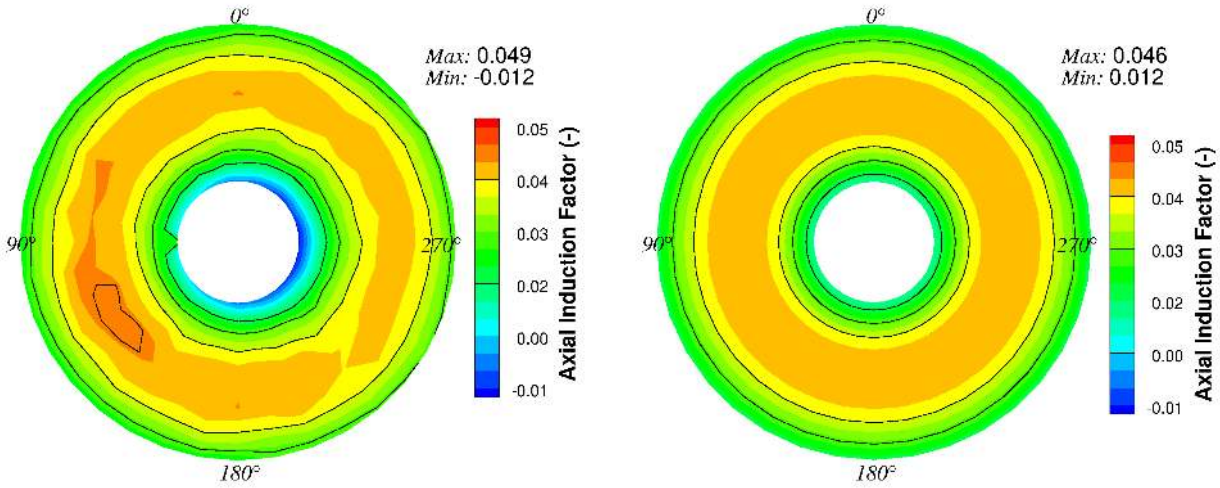

(a) Experiment

(b) CFD, $\beta_{70R} - 2.5°$

Fig. 9 Comparison between the experimental and numerical study, at a reduced pitch of 2.5°**, of the axial induction factor for the axial flow test case.**

Presented in Figure 10, is the computational wake visualised using iso-surfaces of dimensional vorticity magnitude of value $2.77/s$ with contours of radially scaled axial distance. As is observed, the blade tip vortex is captured up until an axial distance of 3.5 R and this preserves the tip vortex well until the 3rd blade passage.

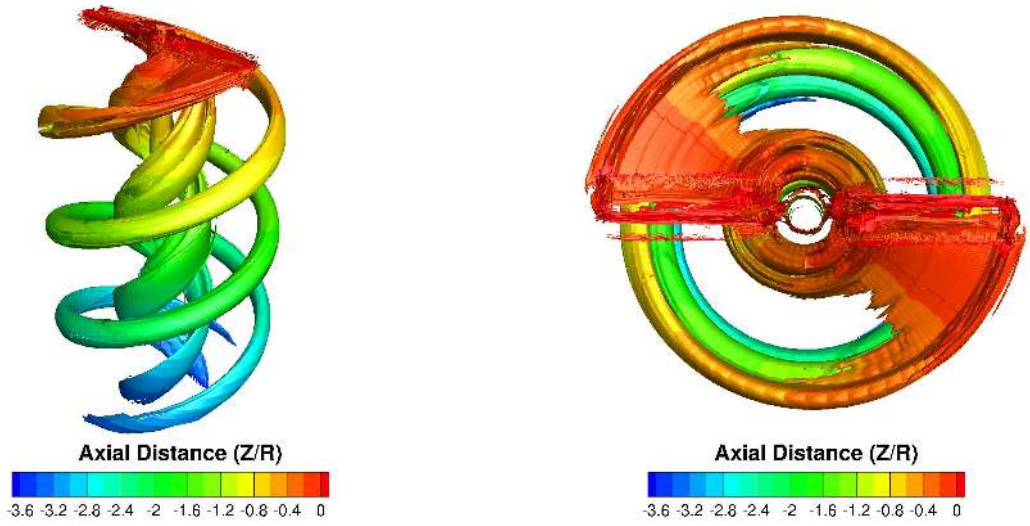

Fig. 10 Flow visualisation of the axial flow computational results using iso-surfaces of $|\vec{\omega}| = 2.77/s$ **with contours of radially scaled axial distance.**

Yawed Flow Conditions

Presented in Figure 11 is the comparison of the axial induction for the 20° yaw case. Very good agreement is found between the experimental and computation results. As per the experiment, there is a 20° shift in the position of maximum induction from the 180° azimuthal location. The negative induction region around the 0° azimuthal station towards the root also agrees well. There is a loss of induction within this section as the wake from the hub interacts with the root flow on the retreating side. In addition to the induction factor trends, the maximum and minimum values also correlate well. In terms of average induction factor, the experimental and CFD data are found to be within 5%, with values of 0.0407 and 0.0426, respectively. This relates to a 5% match in terms of thrust, with values of 7.83 N for the experiment and 8.21 N for the simulation. Therefore, no adjustment of the pitch angle is required. The difference in reference pitch angle, which results in an agreement of thrust, for the yawed and axial conditions is believed to be a result of installation effects.

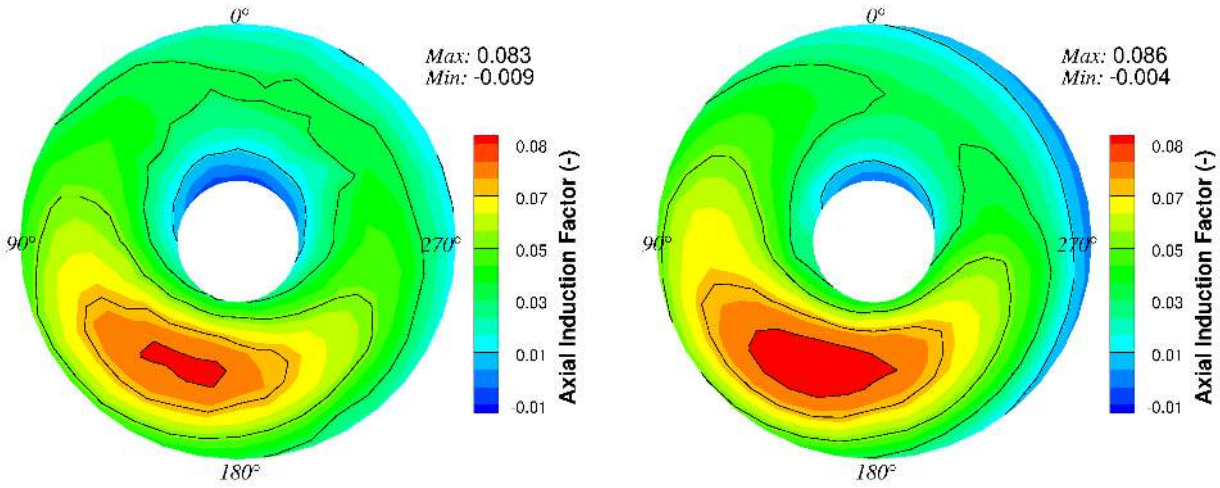

(a) Experiment (b) CFD

Fig. 11 Comparison between the experimental and numerical study of the axial induction factor for the 20° yaw test case.

The introduction of yaw not only increases the overall thrust value for the propeller, but also introduces a variation around the azimuth. As can be seen in Figure 12 and as previously stated, the averaged value obtained from the yawed induced velocity profiles is 8.21 N. The average yawed value obtained from the surface loads is 11.39 N. This is 38.7% greater than the induced profile thrust and is a result of the profile being extracted 3cm from the blade surface. Looking at the instantaneous yawed values from the surface loads, a variation in load of 5.43 N is observed around the azimuth. This variation is not seen from the axial test case. There is an increase in both the average surface and average induced profile thrust with the introduction of yaw. This is to be expected at a given advance ratio based upon previous findings in literature [34].

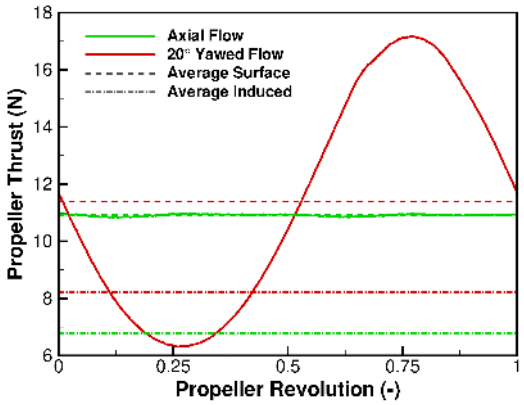

Fig. 12 Variation of propeller thrust due to the introduction of yawed flow.

In addition to the axial induction factors, the radial and tangential components are compared in Figures 13 and 14, respectively. Looking at the radial induction factor, a similar azimuthal shift in the profile as the axial induction is observed. The maximum radial induction is found at the 180° location, with the higher induction values above 0.02 projected round to the 90° station due to the yawed freestream flow. As per the axial case and looking at the 180° station, the radial induction reduced around the mid-span and is negligible up until the 70% radial station. From the 70% station to the tip, the radial induction increases to negative values, projecting the flow towards the root. A similar profile is observed over the disk, with lower values of radial induction found around the 45° station.

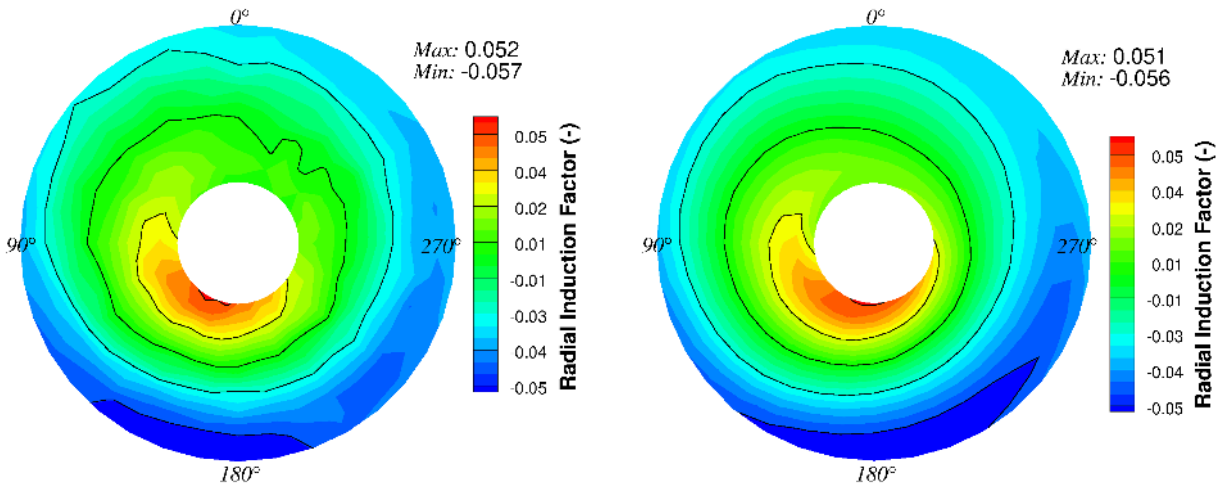

(a) Experiment (b) CFD

Fig. 13 Comparison between the experimental and numerical study of the radial induction factor for the 20° **yaw test case.**

The tangential induction factor (Figure 14) shows very good agreement between the experimental and CFD results. An inverted symmetric profile is observed, with the positions of the maximum and minimum shifted in a clockwise

manner from the 90° and 270° station, respectively. The tangential induction factor has the smallest influence on the induced flow, however, becomes more influential at yaw, as observed from the profiles.

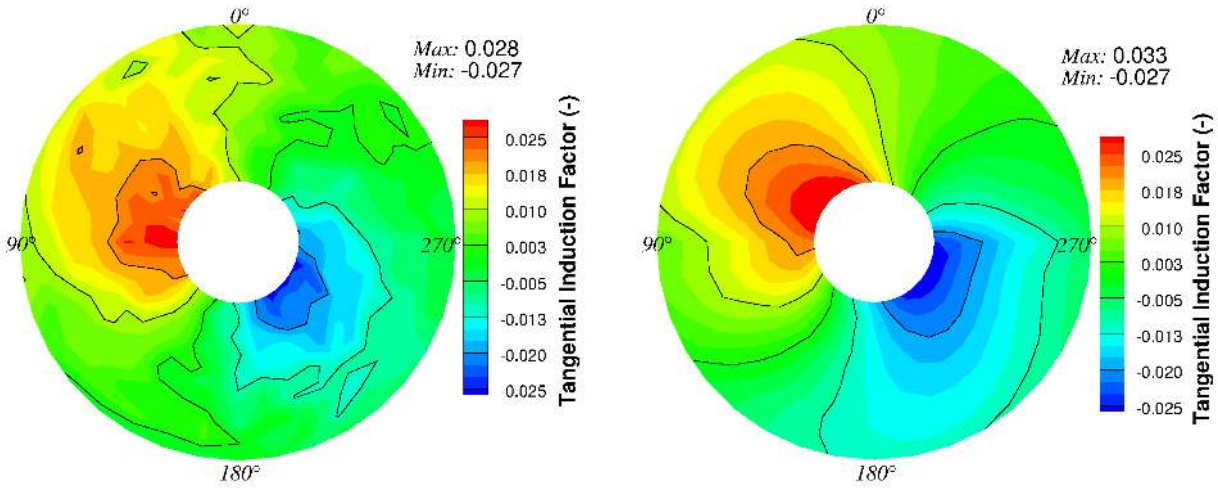

(a) Experiment (b) CFD

Fig. 14 Comparison between the experimental and numerical study of the tangential induction factor for the 20° yaw test case.

Presented in Figure 15 is the derived computational wake visualised using iso-surfaces of dimensional vorticity magnitude of value $2.77/s$ with contours of radially scaled axial distance. As is observed, the blade tip vortex is captured up until an axial distance of 3.5 R and this preserves the tip vortex well until the 3rd blade passage. Based upon these comparisons, it is clear that CFD is able to capture the effect of yawed inflow to a propeller.

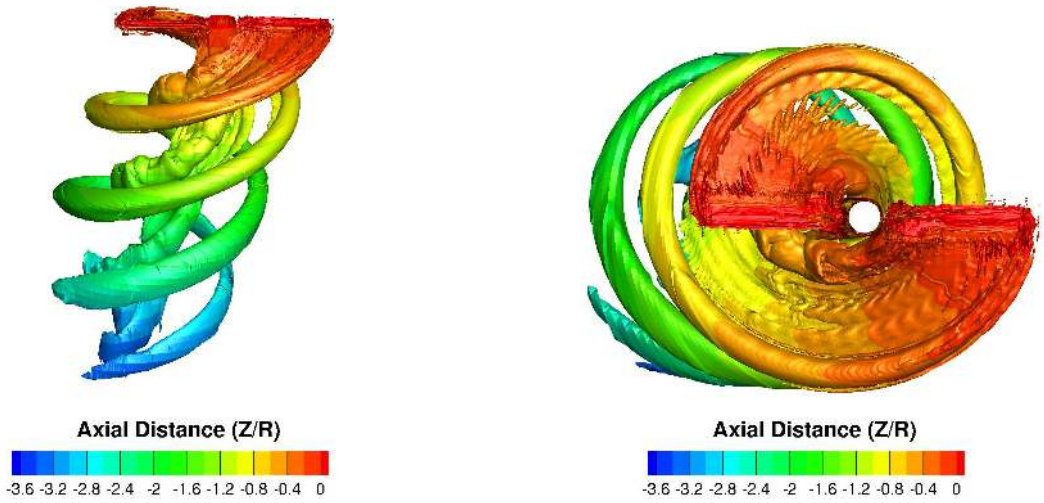

Fig. 15 Flow visualisation of the 20° yaw computational results using iso-surfaces of $|\vec{\omega}| = 2.77/s$ with contours of radially scaled axial distance.

Effect of yaw on blade skin friction

Presented in Figure 16 is the change in vertical viscous load between the axial and yawed test cases. As observed, a sinusoidal variation in viscous loads is seen between the two test cases. This is a result of how the incoming yawed flow interacts with the accelerated flow over the blade.

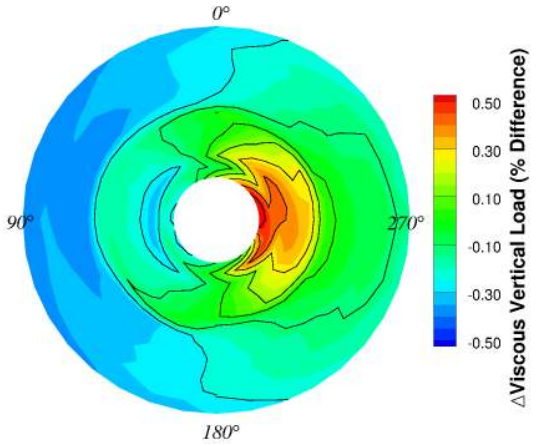

Fig. 16 Non-dimensional viscous vertical load over an entire blade around a single propeller revolution. Comparison between the axial and yawed test case.

The change in tangential velocity between the axial and yawed cases at 90° and 270° is shown in Figure 17. These stations highlight the effect of the incoming yawed flow on the blade loads. Looking at the 90° station (Figure 17(a)), a clear reduction in the velocity across the blade upper surface is observed. This is due to the inflow opposing the accelerated flow over the blade. The opposite is true at the 270° station (Figure 17(b)), where the incoming flow combines with the blade induced velocity to increase the overall speed over the blade surface.

Following this, the skin friction details for the axial and yawed test cases at 90° and 270° are presented in Figure 18. For the axial flow case, an almost linear drop in skin friction is seen across the chord, with a slight increase at the trailing edge towards tip due to the acceleration of the flow over the trailing edge profile. This profile is kept almost constant throughout the entire simulation. The introduction of yaw increases overall levels of skin friction due to the additional cross-flow velocity component. A variation in the skin friction levels is also seen around the revolution due to the influence of the freestream flow. The reduced acceleration seen at the 90° station reduces the overall level of skin friction at the leading edge. The opposite applies at the 270° station where the skin friction level increases due to the increased velocity.

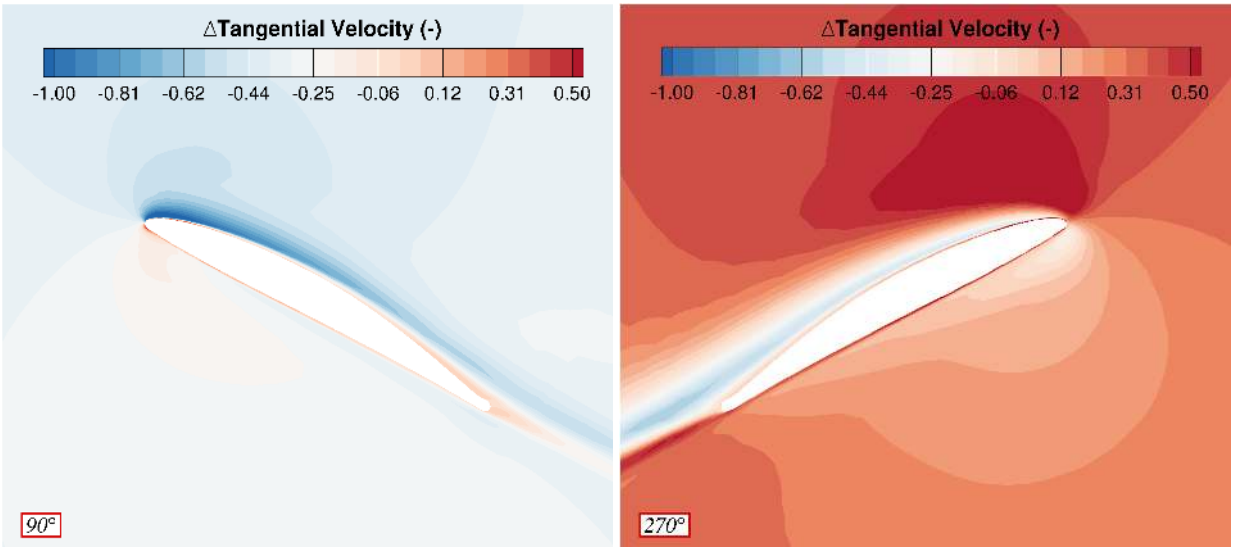

(a) 90° (b) 270°

Fig. 17 Comparison of the change in tangential velocity profiles between the axial and yawed cases at 90° and 270° azimuth.

Based upon these results, it is clear that viscous effects increase in importance due to the change in inflow angle. Therefore, any numerical investigation into such flow must take into account viscosity, as is done for this CFD investigation.

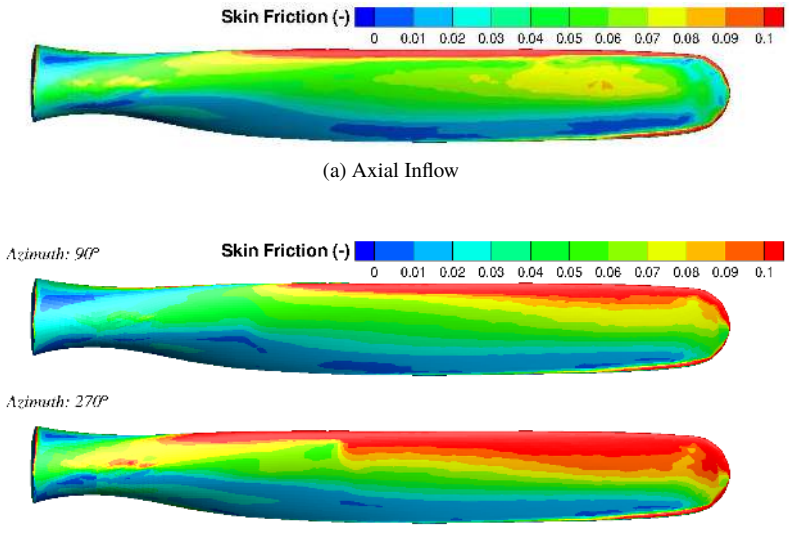

(a) Axial Inflow

(b) Yawed Inflow

Fig. 18 Comparison of the skin friction coefficient for the axial and yawed test cases.

Induced Angle of Attack

The introduction of a freestream yaw angle results in a change in propeller pressure loading around the azimuth. This change in loading is a result of the change in induced angle of attack seen by the propeller. To estimate the change in induced angle of attack between the axial and yawed simulations, a series of steady two-dimensional aerofoil calculations were conducted in order to estimate the normal force coefficient associated with a given radial station.

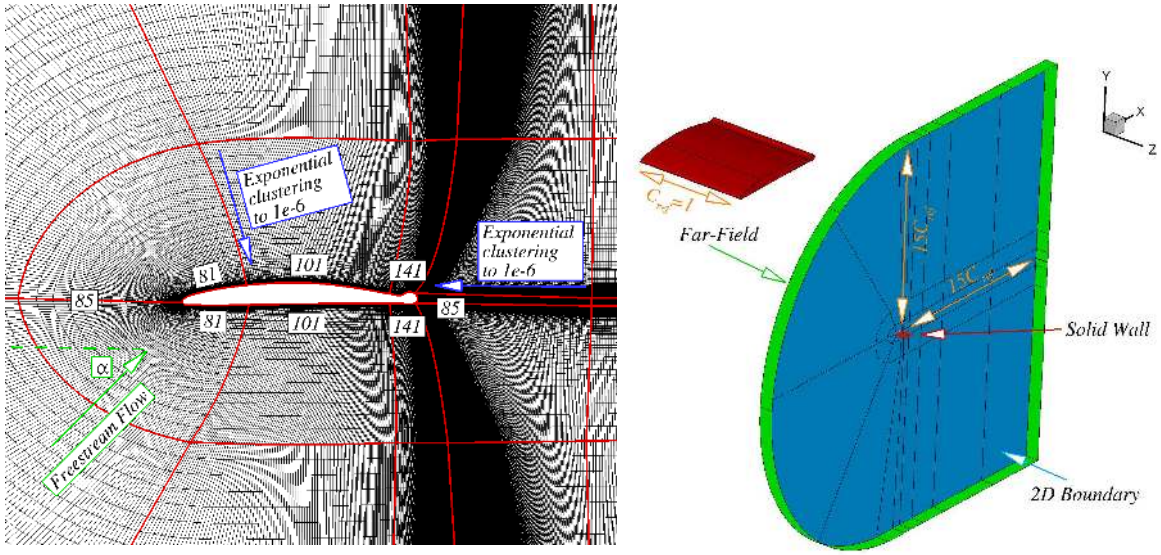

Fig. 19 Two-dimensional aerofoil mesh topology and node distribution around the aerofoil.

For the two-dimensional simulations, a matched grid of $0.25M$ cells is derived for the 50% to 90% radial stations. Presented in Figure 19 is the mesh topology and node distribution around the aerofoil. These are kept constant for all radial stations with slight adjustments made at the trailing edge due to the aerofoil profiles. Far-field boundary conditions are applied 15 chord lengths from the solid aerofoil, with the spanwise distance selected as a single chord length. Two-dimensional boundary conditions are applied to the spanwise faces of the domain with a single cell in the spanwise direction.

RANS computations, coupled with the $k-\omega$ turbulence model, are conducted over a range of incidence angles. The incidence changes are applied via the freestream flow and range from below the zero lift angle up until stall. The reference Mach number and Reynolds number were selected based upon the local conditions exhibited by the 3D propeller blade.

Presented in Figure 20 are the 2D aerofoil results used to compare with the 3D sectional loads. The 3D loads are estimated using the local dynamic pressure to obtain the normal force component. These are then compared with the 2D loads to obtain an effective angle of attack. This is subtracted from the geometric pitch to obtain the induced pitch angle.

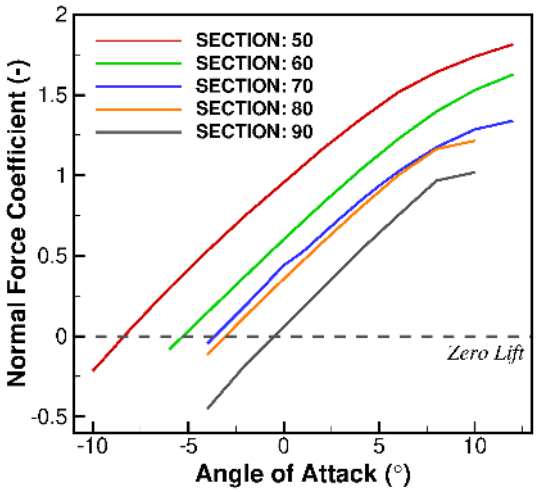

Fig. 20 Two-dimensional aerofoil normal force coefficient results for the 50% to 90% radial stations.

Presented in Figure 21 is the change in induced angle of attack due to the introduction of a yawed inflow. The introduction of a yaw angle causes an overall increase in the induced angle of attack throughout the entire propeller revolution due to the increase in radial velocity. There is also a sinusoidal variation in the induced angle. In a similar manner to the viscous loads, this is a result of the change in flow-field acceleration over the blade.

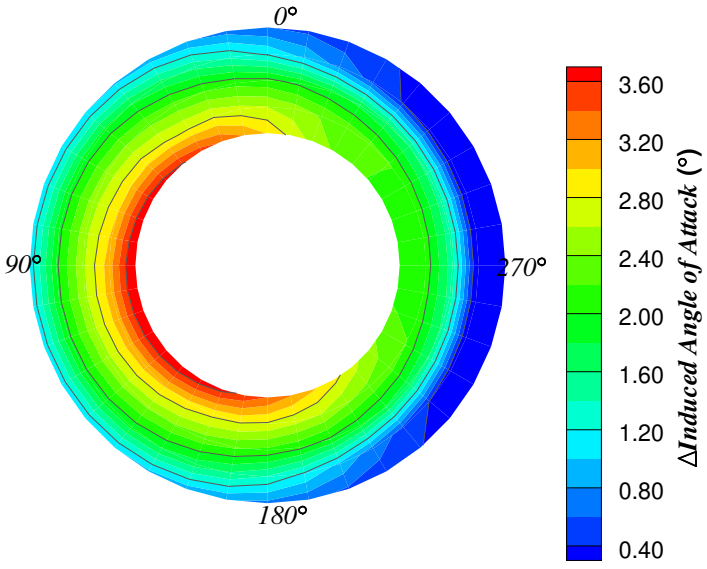

Fig. 21 Difference in induced angle of attack for the axial versus yawed test case.

Conclusions

The following conclusions are observed from this investigation:

A grid convergence and turbulence study was conducted which demonstrated good convergence of the numerical data. For future study and experimental comparisons, the baseline grid utilised the *URANS* formulation closed with the $k-\omega$ turbulence model.

It was found that in order to observe accurate comparisons between CFD and experiments in terms of inflow profiles, the same level of thrust must be generated. This was shown for the axial flow case where the pitch angle had to be reduced by 2.5° in order to match thrust and induction factor levels.

A very good agreement is found between the experimental results and CFD when in yawed conditions. As concluded within the experimental investigation, the introduction of incidence alters the azimuthal position of maximum induction. Some known numerical models fail to capture this shift and, therefore, highlight the ability of the CFD to accurately capture propeller inflow features.

The effect of a freestream yaw angle on the induced angle of attack and skin friction is presented, with a sinusoidal variation observed around the azimuth. This sinusoidal variation in induced angle of attack and skin friction is a result of the change in flow-field acceleration over the blade. It is also shown that the role of viscosity becomes more important with changes in freestream angle, therefore, any numerical simulation must take this into account when studying such flows.

Acknowledgments

The support provided by The Engineering and Physical Sciences Research Council (EPSRC), the Aircraft Research Association (ARA), the National Wind Tunnel Facility (NWTF) of the United Kingdom and the U.K. Vertical Lift Network (UKVLN) is gratefully acknowledged.

References

[1] Chirico, G., Barakos, G., and Bown, N., "Numerical aeroacoustic analysis of propeller designs," *The Aeronautical Journal*, Vol. 122, No. 1248, 2018, pp. 283–315. DOI: https://doi.org/10.1017/aer.2017.123.

[2] Steijl, R., Barakos, G. N., and Badcock, K., "A framework for CFD analysis of helicopter rotors in hover and forward flight," *International Journal for Numerical Methods in Fluids 2006*, Vol. 51, No. 8, 2006, pp. 819–847. DOI: https://doi.org/10.1002/d.1086.

[3] Leble, V., and Barakos, G., "Demonstration of a coupled floating offshore wind turbine analysis with high-fidelity methods," *Journal of Fluids and Structures*, Vol. 62, 2016, pp. 272–293. DOI: https://doi.org/10.1016/j.jfluidstructs.2016.02.001.

[4] Shahpar, S., "SOPHY: An Integrated CFD BASED Automatic Design Optimisation System," *International Symposium on Air Breathing Engines, Munich, Germany.*, American Institute of Aeronautics and Astronautics, 2005. ISBN: 9781563477904.

[5] Zarev, A., and Green, R., "Experimental investigation of a two-bladed propeller at incidence," *Aerospace Science and Technology (Submitted for publication)*, 2019.

[6] Bramwell, F., Relf, E., and Bryant, L., "Experiments on model propeller at the national physical laboratoy, (ii) experiments to determine the lateral force on a propeller in a side wind," Tech. Rep. 123, British ACA, 1914.

[7] Durand, W., and Lesley, E., "Tests on Air Propellers in Yaw," Tech. Rep. 113, National Advisory Committee for Aeronautics, 1923.

[8] Flachsbart, O., and Krober, G., "Experimental Investigation of Aircraft Propellers Exposed to Oblique Air Currents," Tech. Rep. 562, National Advisory Committee for Aeronautics, 1930.

[9] Freeman, H., "The effect of small angles of yaw and pitch on the characteristics of airplane propellers," Tech. Rep. 389, National Advisory Committee for Aeronautics, 1932.

[10] Harris, R., "Forces on propeller due to sideslip," Tech. Rep. 427, British Aeronautcal Research Council, 1918.

[11] Lesley, E., Worley, G., and Moy, S., "Air Propellers in Yaw," Tech. Rep. 597, National Advisory Committee for Aeronautics, 1937.

[12] Gray, W., Jr., J. H., and Jr., A. H., "A wind-tunnel investigation of the effects of thrust axis-inclination on propeller first-order vibration," Tech. Rep. 1205, National Advisory Committee for Aeronautics, 1954.

[13] Pendley, R., "Effect of propeller-axis angle of attack on thrust distribution over the propeller disk in relation to wake-survey measurement of thrust," Wartime Report L-517, National Advisory Committee for Aeronautics, 1943.

[14] McLemore, H., and Cannon, M., "Aerodynamic investigation of a four-bladed propeller operating through an angle-of-attack range from 0 to 180," NACA TN 3228, National Advisory Committee for Aeronautics, 1954.

[15] Russell, J., "Wake survey and strain-gauge measurements on an inclined propeller in the R.A.E. 24-ft tunnel: Part I: Wake Survey," Tech. Rep. 648, British Aeronautcal Research Council, 1953.

[16] Russell, J., "Wake survey and strain-gauge measurements on an inclined propeller in the R.A.E. 24-ft tunnel: Part 2: Strain-gauge measurements," Tech. Rep. 648, British Aeronautcal Research Council, 1953.

[17] Yaggy, P., and Rogallo, V., "A wind-tunnel investigation of three propellers through an angle of attack from 0 to 85," NACA TN D-318, National Aeronautics and Space Administration, 1960.

[18] Young, J. D., "Propeller at High Incidence," *Journal of Aircraft*, Vol. 2, No. 3, 1965. DOI: https://doi.org/10.2514/3.43646.

[19] Crigler, J., and J. Gilman, J., "Calculation of Aerodynamic Forces on a Propeller in Pitch or Yaw," Tech. Rep. 2585, National Aeronautics and Space Administration, 1952.

[20] Pitt, D., "Rotor Dynamic Inflow Derivatives and Time Constants from Various Inflow Models." Tech. Rep. 81-2, Army Troop Support and Aviation Material Readiness Command, 1980.

[21] Peters, D., and HaQuang, N., "Dynamic inflow for practical applications," *Journal of the American Helicopter Society*, Vol. 33, No. 4, 1988. DOI: https://doi.org/10.4050/JAHS.33.64.

[22] Leng, Y., Yoo, H., Jardin, T., Bronz, M., and Moschetta, J.-M., "Aerodynamic Modelling of Propeller Forces and Moments at High Angle of Incidence," *AIAA SciTech Forum, San Diego, California, USA*, 2019. DOI: https://doi.org/10.2514/6.2019-1332.

[23] Dehaeze, F., and Barakos, G., "Mesh deformation method for rotor flows," *Journal of Aircraft*, Vol. 49, No. 1, 2012, pp. 82–92. DOI: https://doi.org/10.2514/1.C031251.

[24] Crozon, C., Steijl, R., and Barakos, G., "Coupled flight dynamics and CFD - demonstration for helicopters in shipborne environment," *The Aeronautical Journal*, Vol. 122, No. 1247, 2018, pp. 42–82. DOI: https://doi.org/10.1017/aer.2017.112.

[25] Babu, S., Loupy, G., Dehaeze, F., Barakos, G., and Taylor, N., "Aeroelastic simulations of stores in weapon bays using Detached-Eddy Simulation," *Journal of Fluids and Structures*, Vol. 66, 2016, pp. 207–228. DOI: https://doi.org/10.1016/j.jfluidstructs.2016.07.014.

[26] Scrase, N., and Maina, M., "The Evaluation of Propeller Aero-acoustic Design Methods by Means of Scaled-Model Testing Employing Pressure Tapped Blades and Spinner," *19th ICAS Congress, Anaheim, California, USA.*, International Council of the Aeronautical Sciences, 1994. ISBN: 1563470845.

[27] Gomariz-Sancha, A., Maina, M., and Peace, A., "Analysis of propeller-airframe interaction effects through a combined numerical simulation and wind-tunnel testing approach," *53rd AIAA Aerospace Sciences Meeting*, AIAA, Kissimmee, Florida, 2015. DOI: https://doi.org/10.2514/6.2015-1026.

[28] Knepper, A., and Bown, N., "IMPACTA Wind-tunnel Instrumentation Specification," Tech. Rep. ITS 01777, Issue 3, Dowty Propellers (GE Aviation Systems Ltd), 2014.

[29] Barakos, G., and Johnson, C., "Acoustic comparison of propellers," *International Journal of Aeroacoustics*, Vol. 15, No. 6-7, 2016, pp. 575–594. DOI: https://doi.org/10.1177/1475472X16659214.

[30] Jarkowski, M., Woodgate, M., Barakos, G., and Rokicki, J., "Towards Consistent Hybrid Overset Mesh Methods for Rotorcraft CFD," *International Journal for Numerical Methods in Fluids*, Vol. 74, No. 8, 2014, pp. 543–576. DOI: https://doi.org/10.1002/fld.3861.

[31] Babu, S., Zografakis, G., Barakos, G., and Kusyumov, A., "Evaluation of scale-adaptive simulation for transonic cavity flows," *International Journal of Engineering Systems Modelling and Simulation*, Vol. 8, No. 2, 2016. DOI: https://doi.org/10.1504/IJESMS.2016.075510.

[32] Loupy, G., Barakos, G., and Taylor, N., "Multi-disciplinary simulations of stores in weapon bays using scale adaptive simulation," *Journal of Fluids and Structures*, Vol. 81, 2018. DOI: https://doi.org/10.1016/j.jfluidstructs.2018.05.012.

[33] Higgins, R., Barakos, G., and Bown, N., "A Time-Marching Aeroelastic Method Applied to Propeller Flutter," *AIAA SciTech Forum, San Diego, California, USA*, 2019. DOI: https://doi.org/10.2514/6.2019-1102.

[34] Serrano, D., Ren, M., Qureshi, A. J., and Ghaemi, S., "Effect of disk angle-of-attack on aerodynamic performance of small propellers," *Aerospace Science and Technology*, Vol. 92, 2019. DOI: https://doi.org/10.1016/j.ast.2019.07.022.